


## ORIGINAL ARTICLE

# Microstructural evolution and texture analysis of magnesium phosphate cement

Alberto Viani<sup>1</sup>  | Gabriele Lanzafame<sup>2</sup> | Daniel Chateigner<sup>3</sup> | Yassine El Mendili<sup>4</sup> | Konstantinos Sotiriadis<sup>1</sup> | Lucia Mancini<sup>2</sup> | Michele Zucali<sup>5</sup> | Bachir Ouladdiaf<sup>6</sup>

<sup>1</sup>Institute of Theoretical and Applied Mechanics of the Czech Academy of Sciences, Prague, Czechia

<sup>2</sup>Elettra-Sincrotrone Trieste S.C.p.A., Trieste, Basovizza, Italy

<sup>3</sup>Normandie Université, CRISMAT-ENSICAEN and IUT-Caen, Université de Caen Normandie, Caen, France

<sup>4</sup>École Supérieure d'Ingénierie et des Travaux de la Construction de Caen (ESITC Caen), Epron, France

<sup>5</sup>Dipartimento di Scienze della Terra "A. Desio", Università degli Studi di Milano, Milan, Italy

<sup>6</sup>Institut Laue Langevin, Grenoble cedex 9, France

## Correspondence

Alberto Viani, Institute of Theoretical and Applied Mechanics of the Czech Academy of Sciences, Centre of Excellence Telč, Batelovská 485, CZ-58856 Telč, Czechia. Email: viani@itam.cas.cz

## Funding information

CERIC-ERIC Consortium

## Abstract

Three-dimensional quantitative image analysis from synchrotron X-ray micro-computed tomography indicated a coarsening of the microstructure of magnesium potassium phosphate cements driven by crystallization of K-struvite from the first amorphous product. Porosity and pore surface area increased because of the progressive build-up of a network of elongated/tabular crystal domains, with density higher than the amorphous. The known increase in strength with time is thought to occur thanks to the overwhelming contribution of a developing interlocked lath-shaped microstructure. Combined X-ray and neutron diffraction texture analysis indicated that at least a fraction of K-struvite nucleates at the surface of MgO grains, suggesting the intervention of more than one crystallization mechanism. The detected weak texture, compatible with a nearly random orientation of crystallites, and the isotropic pore fabric, are beneficial with respect to crack propagation.

## KEYWORDS

microstructure, pores/porosity, texture, X-ray computed tomography, X-ray methods

## 1 | INTRODUCTION

Despite the large body of literature on magnesium phosphate cements, a class of chemically bonded ceramics, there is still insufficient information about microstructure development and its connection with parameters of cement formulation and, ultimately, the reaction mechanisms.

Hardening of magnesium potassium phosphate cements (MPCs) occurs at room temperature through the acid-base aqueous reaction between magnesium oxide (MgO, periclase) and potassium dihydrogen phosphate (KH<sub>2</sub>PO<sub>4</sub>). The reaction is reported to produce K-struvite (MgKPO<sub>4</sub>·6H<sub>2</sub>O).

Cement performance has been shown to depend upon the magnesia-to-phosphate molar ratio, water-to-solid weight

ratio, grain-size distribution, and reactivity of MgO.<sup>1–4</sup> Comparison between results of the numerous studies on MPCs has been severely hampered by the wide variations in the use of retarders, amount of water, and typology of MgO.<sup>5</sup> In a series of papers, we have studied the role of MgO reactivity in affecting the cement properties to gain insights into the mechanisms of the reaction, as key to product design.<sup>6–12</sup> In fact, MgO dissolution is the first reaction step, driven by the acidic environment established by the fast dissolution of the acid phosphate in water.<sup>13</sup> The availability of Mg<sup>2+</sup> promotes the formation of solid reaction products. Despite a solid mass is obtained few minutes after mixing, most of the strength development is delayed and occurs over a long time scale (several days).<sup>2,3,8,14</sup> Such behavior has been attributed

to the formation of an amorphous/paracrystalline intermediate reaction product, precursor of K-struvite.<sup>12,15</sup> Correlation of mechanical performance with amount of K-struvite,<sup>8,14</sup> indicated in the progressive development of a pervasive network of tabular/elongated K-struvite crystals the main toughening mechanism in MPCs.<sup>8,16</sup>

As recently probed for MPC formulations in a range of water-to-solid weight ratios using Synchrotron X-ray microComputed Tomography (mCT),<sup>17</sup> the amorphous-to-crystalline transformation, which is always incomplete, plays a central role in dictating the development of the microstructure and, ultimately, the performance of the cement, establishing the link between reaction mechanisms and properties.

In order to clarify the conflicting evidences on the development of porosity<sup>1,17,18</sup> and prove/disprove the models of microstructural evolution of MPCs,<sup>1</sup> in this work, the microstructure of MPC produced from MgO sintered at three different temperatures and its time-evolution have been described in a fully non-destructive fashion with mCT.

Moreover, since the elongated and/or platelet-like crystal habit of K-struvite, which characterizes the fabric of MPCs, in principle might lead to anisotropy of physical properties, both neutron and X-ray diffraction experiments have been conducted to examine sample texture, coherent domain sizes and shapes, microstrains, and structural variations.

## 2 | EXPERIMENTAL PROGRAMME

### 2.1 | Materials and cement preparation

Three MgO powders, already employed in MPCs,<sup>8,11,12</sup> were produced by annealing, in electrical furnace, pharmaceutical grade MgCO<sub>3</sub> at 1500°C, 1550°C, and 1600°C for 40 minutes. The MgO powders were then milled for 2 minutes in a Mini-Mill Pulverisette 23 (Fritsch) at 30 oscillations/min and stored in a desiccator until use. Particle size analysis was conducted on triplicates, resulting in a BET surface area of 4.5 m<sup>2</sup>g<sup>-1</sup> and average particle size  $d_{50} = 3.9 \mu\text{m}$ ; 2.4 m<sup>2</sup>g<sup>-1</sup> and  $d_{50} = 4.2 \mu\text{m}$ ; 0.9 m<sup>2</sup>g<sup>-1</sup> and  $d_{50} = 5.5 \mu\text{m}$ , for samples annealed at 1500°C, 1550°C, and 1600°C, respectively. MPC samples with magnesia-to-phosphate molar ratio of 1.75 (with respect to the stoichiometry of the reaction, 10.2 wt% of the mix will be unreacted MgO) and water-to-solid weight ratio of 0.44, were prepared at 20°C by mixing for 20 seconds MgO powder with KH<sub>2</sub>PO<sub>4</sub> and water. Samples for mCT measurements were casted in form of cylinders (3.8 mm diameter, about 20 mm height) and kept sealed in plastic bags at 20°C until testing and covered with Parafilm M<sup>®</sup> to prevent water loss during measurement. Sample for texture measurements with neutrons has been prepared using the same molar amount of D<sub>2</sub>O in place of water to reduce the

contribution from incoherent scattering of H. The samples have been shaped in the form of cubes (1 cm edge).

The naming convention of the MPC samples followed throughout this paper is MPC\_X\_Y, where X is the sintering temperature of MgO and Y is the aging time (1 hour, 4 hours, 9 hours, 12 hours, 21 hours, and 15 days).

### 2.2 | mCT measurements

#### 2.2.1 | Experiments

mCT measurements have been performed at SYRMEP beamline of the Elettra Sincrotrone Trieste in Basovizza (Italy) employing a filter-hardened (1.5 mm Si + 1 mm Al) white X-ray beam.

Samples aged 15 days were measured acquiring 1800 radiographic images (projections) over an angular range of 180° and with an exposure time/projection of 1.5 seconds. Time-resolved experiments were carried out acquiring 900 projections over an angular range of 180° with an exposure time/projection of 1.0 seconds, for each sample MPC\_1500 and MPC\_1550, at 1 hour, 4 hours, 9 hours, 12 hours, and 21 hours after mixing. The dataset MPC\_1550\_21 hours has been excluded from the analysis because incomplete.

The mCT scans have been collected by *local area* or *region-of-interest* mode<sup>19</sup> on a 16-bit 2048 × 2048 pixels sCMOS camera. The effective pixel size of the detector was set at 0.9 μm × 0.9 μm, yielding a maximum field of view of about 1.8 mm × 1.8 mm. The propagation-based phase-contrast mode was adopted.<sup>20</sup> The sample-to-detector distance was set to 80 mm.

The tomographic reconstruction was performed using the SYRMEP Tomo Project software provided by Elettra. A single-distance, phase-retrieval algorithm was applied to the sample projection images. Optimal ratio between the real and imaginary parts of the refractive index in the samples was set to 40.

#### 2.2.2 | Processing and analysis of mCT images

*Pore3D* software library<sup>21</sup> was employed for processing and quantitative analysis of the reconstructed volumes. The softwares Fiji<sup>22</sup> and VGStudio 3.0 (Volume Graphics) were adopted to visualize the as reconstructed or processed bi-dimensional (2D) slices and 3D visualization, respectively.

Image segmentation, aimed at extracting the pores from the matrix, has been performed applying a 3D anisotropic diffusion filter followed by the automatic 3D Otsu segmentation algorithm (both implemented in *Pore3D*). The more computationally intensive quantitative image analysis was conducted on a Volume Of Interest (VOI) representing the investigated sample, and defined from the Representative

Elementary Volumes (REVs) obtained for each sample<sup>23</sup> (see Figure S1).

A VOI of  $1280 \times 1280 \times 1280$  voxels (larger than the REV), corresponding to a volume of  $1.529 \text{ mm}^3$ , common to all samples, was chosen. For a meaningful description of the VOI, voids with volume less than  $27 (3 \times 3 \times 3)$  voxels (volume size  $< 19.7 \mu\text{m}^3$ ) have been excluded from the quantitative analysis. Separation of connected pores was evaluated first, by extracting largest pores in each VOI. They resulted small in size with only minor and sporadic connections (Figure S2). Therefore, no pore separation procedure (eg watershed) was adopted. The following parameters, defined in *Pore3D*, were obtained from the quantitative image analysis: porosity ( $\Phi$ ) and distribution of pore volumes; surface area per unit volume ( $S_V$ ); fractal dimension ( $D_F$ ); connectivity density (CD). The skeletonization, which allows for a 1D representation of the 3D pore network preserving its topology,<sup>24</sup> has been conducted by applying the GFV algorithm on the selected VOI.<sup>25</sup> Anisotropy of the pore network was quantified calculating the anisotropy index ( $I$ ) and elongation index ( $E$ ).

### 2.3 | Scanning electron microscopy (SEM)

Scanning electron microscopy images were collected from the freshly fractured surface of specimens. Samples were mounted on an aluminium stub and coated with 5 nm thick gold film. Observation have been conducted with a FEI QUANTA FEG 450 instrument at 20 kV accelerating voltage. A gaseous backscatter electron detector working at 200 Pa pressure was employed in order to limit loss of structural water from the samples.

### 2.4 | X-ray powder diffraction (XRPD)

X-ray powder diffraction data were collected with a Bragg–Brentano  $\theta$ - $\theta$  diffractometer (Bruker D8 Advance, Cu radiation) equipped with a LynxEye 1-D detector, divergence 0.6 mm slit and  $2.5^\circ$  Soller slits on the incident beam; Ni filter (to enhance the  $K_\alpha$  radiation  $\lambda = 1.5418 \text{ \AA}$ ) and  $2.5^\circ$  Soller slits on the diffracted beam. Samples were ground by hand in an agate mortar and mounted on an Al sample holder using the side loading technique to minimize a priori preferred orientation of crystallites. The angular range  $4\text{--}82^\circ 2\theta$  was covered at virtual steps scan of  $0.0102^\circ 2\theta$  with 0.4 s/step counting time at 40 kV and 40 mA, spinning the samples at 15 rpm. Quantitative phase analysis including both amorphous and crystalline fraction was performed with the Rietveld method by spiking the sample with 10 wt% of internal standard (NIST SRM 676a alumina). Rietveld refinements have been accomplished with the TOPAS 4.2 software (Bruker AXS) employing the fundamental parameter approach. The Crystallography Open Database<sup>26</sup> structure models # 9 000 490 and # 9 010 847 were adopted for MgO/

periclase (space group *Fm-3m*) and K-struvite (space group *Pmn2<sub>1</sub>*), respectively.

### 2.5 | Quantitative texture analysis

Crystallographic texture, coherent domain sizes and shapes, microstrains, and structural variations have been investigated using X-ray and neutron diffraction on the sample MPC\_1600\_15 days. While X-ray diffraction probes typically some  $\text{mm}^2$  on the sample surface and few tens of microns in depth, neutron diffraction allows for the investigation of relatively large volumes of sample (around  $1 \text{ cm}^3$ ). For both X-ray and neutron texture experiments, the sample where mounted on the diffractometers in such ways that the sample axis (casting axis) corresponded to the centre of the pole figures.

X-ray texture data have been collected using a four-circles diffractometer setup (Huber goniometer) equipped with a Curved Position Sensitive detector (CPS120 from Thermo Scientific, Artenay, France) using the averaged Cu  $K_\alpha$  radiation from a flat graphite monochromator. The neutron measurements have been performed with the D1B four-circles diffractometer at the high-flux steady-state reactor of the Institute Laue-Langevin (Grenoble, France) using the  $2.526039 \text{ \AA}$  wavelength from the pyrolytic graphite (002) monochromator.<sup>27</sup> Scattered neutrons have been detected with the Curved Position Sensitive detector spanning an angular range of  $128^\circ$ .

X-ray and neutron data were analysed in the framework of the Combined Analysis formalism<sup>28</sup> implemented in the software MAUD,<sup>29</sup> which involves cyclic Rietveld refinement of a series of diffraction patterns measured at different sample orientations. Using X-rays, 864 patterns equally spaced  $5^\circ$  in tilt and azimuthal angles ( $\chi$  and  $\phi$ , respectively) were collected in the range  $0^\circ \leq \chi \leq 55^\circ$  and  $0^\circ \leq \phi \leq 355^\circ$  with 4 min counting time for each sample orientation. Pole figure “blind” areas were reduced by choosing the incident angle of the X-ray beam on the sample surface of  $\omega = 15^\circ$ .<sup>28</sup>

Using neutrons, the  $\phi$  and  $\chi$  increments were of  $10^\circ$ , in the ranges  $0^\circ \leq \chi \leq 90^\circ$  and  $0^\circ \leq \phi \leq 350^\circ$ , with  $\omega = 45^\circ$ , resulting in 360 patterns measuring 1 min each.

The obtained pole figures were normalized into multiples of a random distribution (mrd.), a unit depending on orientation only. The overall texture strength was evaluated through the texture index<sup>30</sup> (in  $\text{mrd}^2$ ), to compare the texture strength of different samples exhibiting similar Orientation Distributions (ODs). Such normalized pole figures are calculated from the OD of crystallites, refined using the E-WIMV algorithm (implemented in MAUD). The OD and profile refinement reliabilities are estimated using conventional reliability factors.<sup>31</sup> The sample reference frame is given by the axis of the small cylinder, centres of the pole figures ( $Z$ ). The instrument contributions were calibrated using the  $\text{LaB}_6$

(NIST SRM 660b) and  $\text{Al}_2\text{O}_3$  (NIST SRM 676b) powder standards for X-ray and neutron data, respectively.

Quantitative phase analysis, unit-cell parameters, crystallite sizes and microstrains, were also refined. The structure of K-struvite was refined from neutron data.

### 3 | RESULTS

In the mCT reconstructed volumes (Figure 1), the following features, according to their range in grey levels, reflecting different contrast for X-rays, were identified:

1. The brightest features are the MgO grains and grain agglomerates.
2. Light grey features, mostly elongated and prismatic, are compatible with the crystal habit of K-struvite,<sup>7</sup> as can be observed from the 3D rendering of one of them isolated from the sample volume (Figure S3). Since the single crystal nature of these individuals cannot be ascertained, we refer to them as “domains” rather than “crystals”.
3. Two other intermediate sources of contrast can be recognised (inset in Figure 1) either as sub-domains of the previous K-struvite habits, or as separated small grains. Such sub-domains, which likely correspond to some form

of chemical inhomogeneity, disappeared during the evolution of the sample.

4. The black areas are pores, characterized by an irregular shape, which, regardless of the annealing temperature of MgO, evolves toward an increasing sharp-cornered outline with time.

Results of quantitative image analysis (Table 1) can be summarized as follows:

1. The detected porosity ( $>19.7 \mu\text{m}^3$ ), increases with time in both samples MPC\_1500 and MPC\_1550.
2. Samples produced with MgO annealed at higher temperature possess, in this pore size range, a more compact microstructure. This is confirmed for 15d-aged samples (Figure S4) and by the fact that at any given aging time,  $\Phi$  is always lower in the sample MPC\_1550, compared to MPC\_1500.
3.  $S_V$  exhibited analogous behavior; sample MPC\_1500 has a larger  $S_V$  than MPC\_1550 at every time during aging, and shows the largest  $S_V$  after 15 days.
4.  $D_F$ , which can be, in first approximation, considered as an indicator of pore-surface roughness,<sup>19</sup> indicated that the pore surface increased its complexity with the progress of the reaction ( $D_F = 2$ , smooth surface;  $D_F = 3$ , irregular or

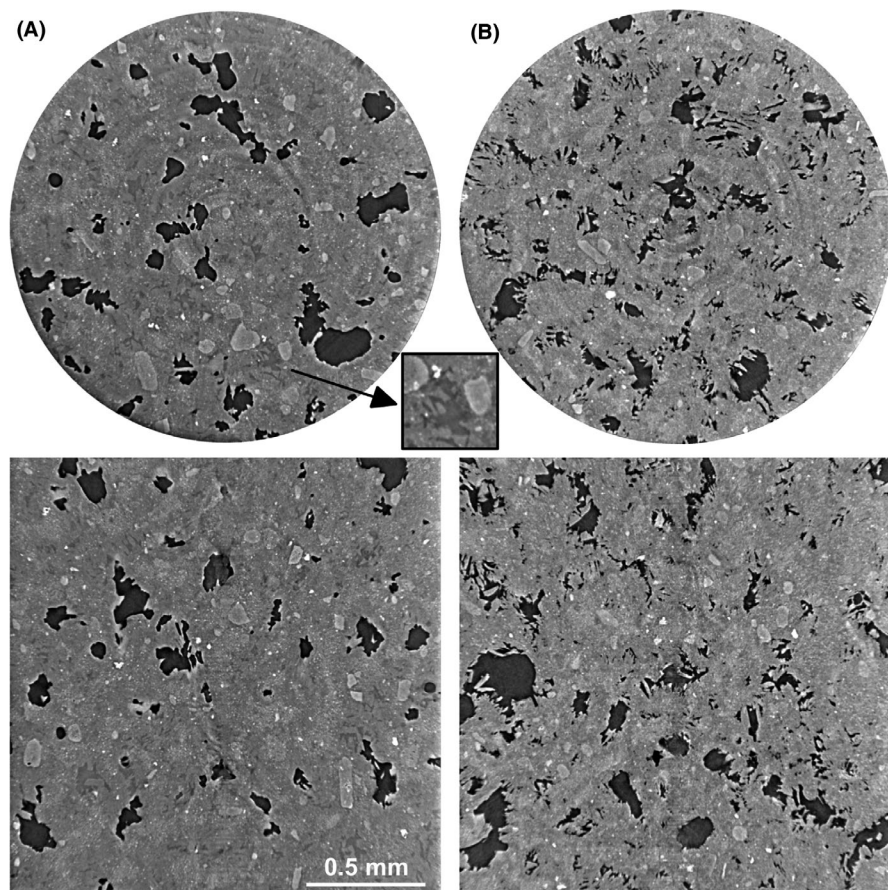


**FIGURE 1** Axial (above) and coronal (below) mCT views of sample MPC\_1500\_1 h (A) and MPC\_1500\_15 d (B). Inset depicts a detail of inhomogeneous area in the sample matrix

**TABLE 1** Results of quantitative image analysis of the pore network for the investigated samples

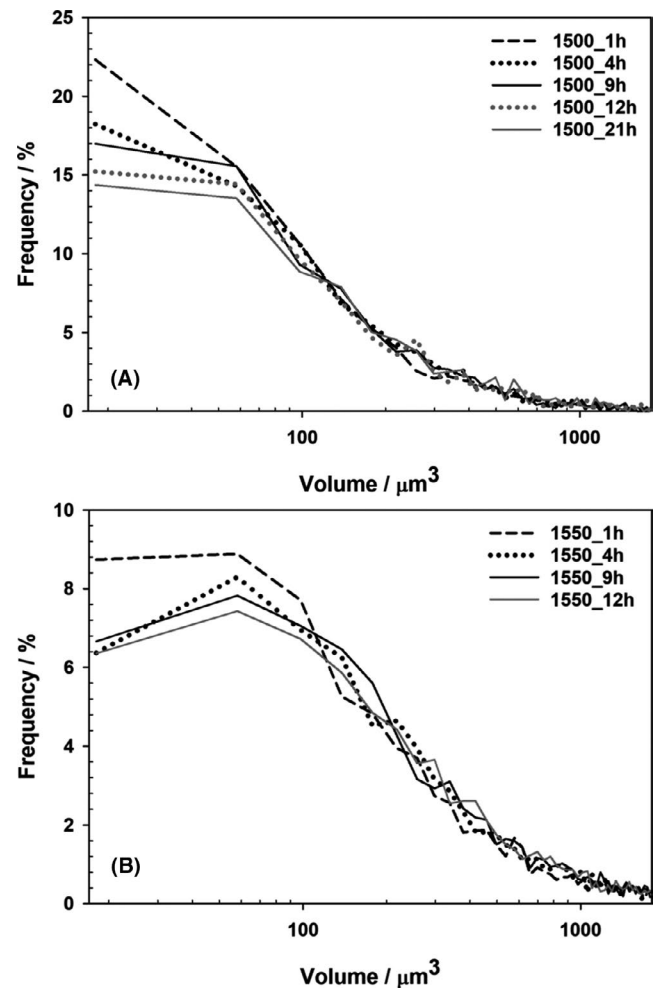
Sample	$\Phi$ (%)	$S_V$ ( $\text{mm}^{-1}$ )	$D_F$	CD ( $\text{mm}^{-3}$ )	$I$	$E$
MPC_1500_1 h	9.9	9.3	2.44	622.7	0.92	0.06
MPC_1500_4 h	10.7	13.2	2.47	1716.3	0.90	0.06
MPC_1500_9 h	12.1	16.7	2.50	2088.5	0.84	0.08
MPC_1500_12 h	11.8	17.0	2.50	1669.2	0.83	0.12
MPC_1500_21 h	12.8	19.2	2.51	2178.8	0.83	0.08
MPC_1500_15 d	14.6	25.4	2.55	1905.4	0.96	0.03
MPC_1550_1 h	2.0	3.9	2.11	53.0	0.90	0.03
MPC_1550_4 h	4.6	7.6	2.29	600.5	0.95	0.01
MPC_1550_9 h	5.0	8.8	2.31	378.1	0.94	0.02
MPC_1550_12 h	5.5	9.8	2.33	349.9	0.93	0.04
MPC_1550_15 d	10.6	17.3	2.48	972.0	0.92	0.02
MPC_1600_15 d	7.8	13.0	2.41	327.7	0.92	0.06

rough surface), and with the increase in sintering temperature of MgO.

5.  $CD$  evidences a striking evolution in the first 4 hours, with an increase in the degree of connectivity of the pore network with time and a decrease when samples at increasing sintering temperature are considered. This is confirmed by the volume rendering of the skeletonized volume (Figure S5) which graphically illustrates the degree of connectivity of the pore network.
6. The values of the isotropy index  $I$ , close to 1, indicate that the pores can be assimilated to a relatively uniform isotropic distribution; very similar values are obtained for the samples after 15 days. Elongation index  $E$  values close to 0 point to a virtually absent preferred orientation.

The detected porosity after 15 days, ranges from 7.8% to 14.6%, values in agreement with a recent work based on mCT data,<sup>17</sup> but higher with respect to most literature, when considering the same range in pore size.<sup>1,3,18</sup> However, direct comparison with some literature data is impaired by differences in the mix formulation and MgO employed. Moreover, the accuracy of results from fluid intrusion methods is questionable, because they are model dependent, limited to the detection of open porosity and, in case of MPC, experimental conditions have been observed to produce irreversible modification of the microstructure.<sup>6</sup>  $S_V$  obtained from Small Angle Neutron Scattering (SANS),<sup>6,8</sup> is 3 orders of magnitude higher, because, as already observed in other phosphate cements,<sup>32</sup>  $S_V$  scales directly with the observation scale.

Figure 2 illustrates the pore-size distribution frequency for samples MPC\_1500 and MPC\_1550 at increasing times. The fine fraction of pores with volumes  $< 200 \mu\text{m}^3$  is by far the most frequent in all the samples. In the sample MPC\_1500 this pore population is more than twice as abundant compared to sample MPC\_1550. During aging,

**FIGURE 2** Time-evolution of pore size distribution frequency for the indicated samples. The range on the large volume side has been limited for sake of clarity

this fine fraction decreases and the distribution shifts toward larger sizes. For example, in the first 12 hours, the number of pores with volume between  $500$  and  $2500 \mu\text{m}^3$ , increases

by 4% in both samples, and the corresponding volume fraction increases.

Results of XRPD quantitative phase analysis and an example of graphical output of the Rietveld refinement, are reported in Table 2 and as Figure S6, respectively. The agreement factors of the refinements, as defined in TOPAS, ranged between  $7.2 < R_{wp} < 7.4$  and  $1.69 < GOF < 1.77$ . The fraction of MgO is constant in all the samples and corresponds well to the estimated unreacted amount<sup>6,8,12</sup>; therefore, according to previous works,<sup>8,12</sup> the changes in phase composition are limited to K-struvite and the amorphous phase. They confirm that the increase in sintering temperature of MgO leads to cements with more K-struvite. The trend is more marked between 1500°C and 1550°C, in agreement with the characteristics of the powders (BET surface area and  $d_{50}$ ), reported above.

Under SEM, the microstructure is dominated by K-struvite domains, arranged in “clusters” of compact stacks of elongated individuals. They can be resolved in proximity of the voids, as illustrated in Figure 3. The pore walls are intersected by large elongated K-struvite domains (up to 40  $\mu\text{m}$  in length), creating a very articulated surface. Such clusters are apparently distributed with random orientation in the cement volume to realize a densely packed interlocked microstructure.

X-ray and neutron Combined Analysis performed on the MPC\_1600\_15 days sample reveals the presence of the two struvite and periclase phases (Table 3) with volume fractions coherent with those obtained from powder diffraction and estimated from the precursor stoichiometry, though neutron data refined to lower periclase content. The diffracted intensity variations with  $(\chi, \phi)$  orientation of the sample were barely visible using X-rays, and a bit more pronounced from the neutron experiments (Figure S7, bottom diagrams). The too much local measurements using X-rays is here of concern. Both experiments exhibit the signature of a weak texture for this sample. Such low textural levels can only be appreciated by refining the three-dimensional orientation distribution. Diagrams obtained from the Combined Analysis refinements correctly reproduced the experimental ones (compare Figure S7, top and bottom sets; Figure S8), with satisfactory reliability factors GOF of  $\sim 2$  and 1.1, respectively. X-rays were used to more precisely define crystallite

sizes and microstrains. Large average crystallite size of periclase, due to high temperature treatment, is in line with literature values.<sup>8</sup> We could not detect any signature of anisotropic shape of the crystallites.

Results of structure refinement of K-struvite from neutron data are reported in Table S1. The obtained D content (10.2 a.f.u.) corresponded well to the expected value (10 a.f.u.), whereas, the mean structure is coherent with already published ones (# 9 010 847 and 9 011 199). Because no reliable results were obtained from the refinement of the texture of periclase, it was assumed to be randomly oriented.

The normalized pole figures calculated from the OD, and reported in Figure 4, indicated a slight orientation strength for the crystallographic texture of struvite, with the main orientation component with the mean c-axis aligned parallel to the normal of the sample. An overall measure of the texture strength (Table 3) is given by  $F^2$  values around 1.01 mrd.<sup>2</sup>. The features at the center of the X-ray {002} pole figure of K-struvite are likely due to graininess. In fact, the crystal sizes are rather large compared to the beam spot size (see Figure 3), therefore limiting the number of irradiated crystals. The minimum OD values for both X-ray and neutron experiments indicate that randomly oriented crystals constitute 67% and 36% of the probed volume, respectively. Consequently, texture variations show locally (in case of X-ray experiments) lower strengths than in the bulk (in case of neutrons). However, the maximum in OD values and the pole figures indicate that such strengths remain close to random orientations.

Looking at the {002} pole figure of K-struvite and {111} pole figure of MgO (Figure 4), an orientation density reinforcement around their center is observed, indicating the alignment of the corresponding crystal directions, within the orientation distribution of these centered poles extending to roughly 20° in  $\chi$ . This is compatible with a topotactic relationship. When considering orientations at 90° in  $\chi$  from these two previous

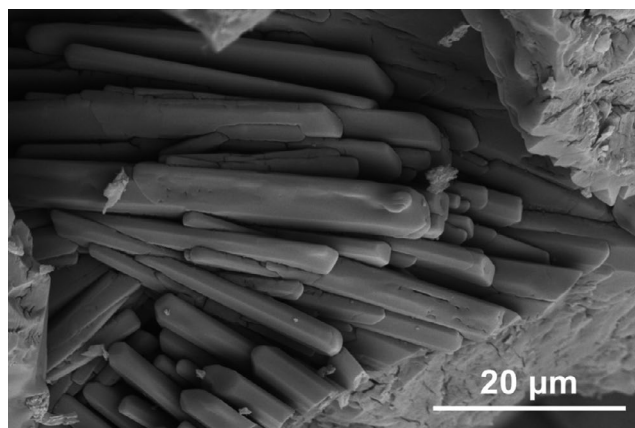


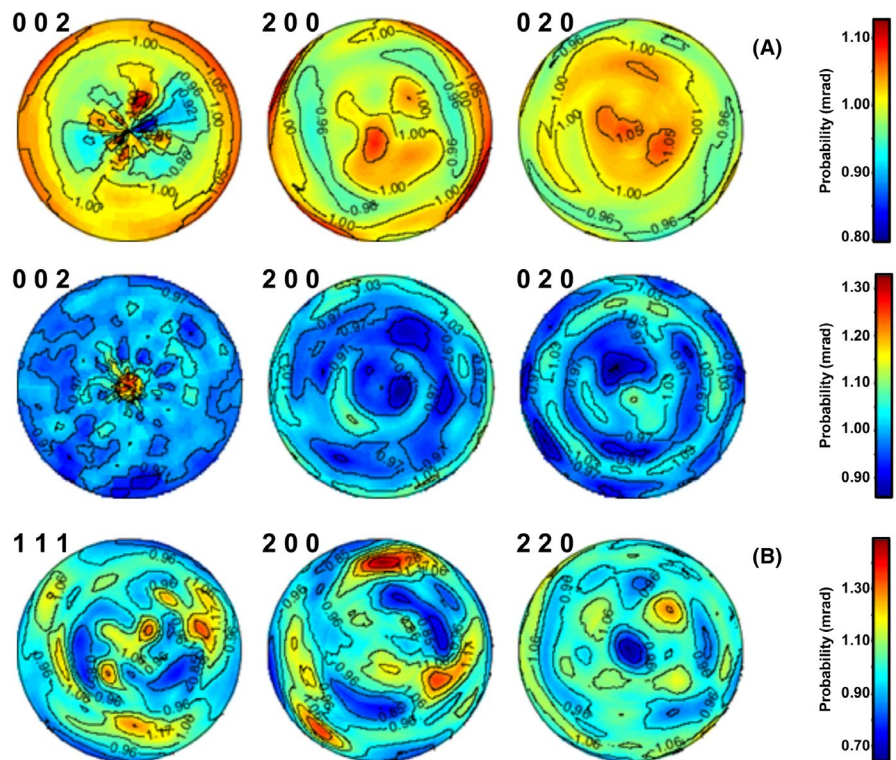
**FIGURE 3** SEM micrograph of the pore internal surface in the sample MPC\_1550\_15 d

**TABLE 2** Quantitative phase analysis results of MPCs samples employed for mCT aged 15 d. Phase fractions are in wt%; standard deviation of the refinement in brackets correspond to  $1\sigma$

Sample	K-struvite	Amorphous	MgO
MPC_1500_15 d	61.0 (1)	30.4 (4)	9.6 (1)
MPC_1550_15 d	67.2 (1)	23.1 (4)	9.7 (1)
MPC_1600_15 d	69.3 (1)	20.8 (4)	9.8 (1)

**TABLE 3** X-ray (top) and neutron (bottom) results of Combined Analysis of the MPC\_1600\_15d sample.  $\langle D \rangle$  is the average crystallite size. Standard deviation ( $1\sigma$  of the calculations, in brackets)

Phases	wt%	Cell parameters (nm)	$\langle D \rangle$ (nm)	Microstrains (r.m.s.)	$F^2$ (mrd.)	OD min (mrd.)	OD max (mrd.)
Periclase	12.3 (5)	$a = 0.425103(4)$ $a = 0.693525(8)$	570 (165)	0.00040 (2)	1.12	0.16	3.30
K-struvite	87.7 (2)	$b = 0.621545(7)$ $c = 1.11918(1)$	163 (9)	0.00055 (1)	1.01	0.67	1.45
Periclase	7.1 (6)	$a = 0.425103(4)$ $a = 0.68692(3)$	320 (185)	0.0018 (3)	—	—	—
K-struvite	92.9 (8)	$b = 0.61554(2)$ $c = 1.0863(3)$	179 (20)	0.0015 (1)	1.01	0.36	2.60

**FIGURE 4** A, Normalized pole figures for the main crystal directions of K-struvite using x-ray (top) and neutron (bottom) diffraction, and of (B) periclase using x-ray diffraction. Equal area projections

directions (ie on the equators of the  $\{200\}$  pole figure of K-struvite and  $\{220\}$  pole figure of MgO), some reinforcements of the orientation densities are observed, but there is no apparent matching of these latter along the  $\phi$  angle, which leads to exclude epitaxial-like relationships. We can conclude that a plane-to-plane overall alignment confirms topotaxy between K-struvite and periclase in the bulk of the material, as seen from neutron diffraction pole figures, but without epitaxial-like relationships. No residual stress, neither compressive nor tensile, could be observed as visible peak shifts with the  $\chi$  angle in our experiments. Therefore, the residual stresses due to K-struvite crystallization process are within the instrumental resolution, that is, smaller than 20 MPa.

## 4 | DISCUSSION

### 4.1 | Time-evolution of MPC microstructure

The first snapshot, after 1 hour (Figure 1), is consistent with the presence of a largely amorphous/poorly crystalline matrix from which K-struvite forms. The progress of crystallization from the amorphous is testified by the geometrical outline of the features illustrated in the inset in Figure 1. Inhomogeneities observed in the volume corroborate the hypothesis of two coexisting amorphous phases, which transform with different rates and from which K-struvite eventually crystallizes, as already indicated by spectroscopy and calorimetry.<sup>9–12</sup> The low viscosity of the slurry

during cement preparation leads us to exclude the possibility of local concentration gradients due to a not perfect mixing. Incomplete dissolution of  $\text{KH}_2\text{PO}_4$ , sometimes reported in MPCs, with this mix composition should be also excluded on the basis of previous results of in-situ and ex-situ XRPD.<sup>7,8,10</sup>

On a smaller size range, but similar samples, SANS indicated that structural changes are mostly concentrated in the first 20-30 minutes, resulting in a decrease of the fine porosity, down to  $\leq 1\%$ .<sup>6,8</sup> A coarsening of the pore-matrix microstructure occurred during the reaction and most of the porosity shifted in time outside the upper limit in size accessed ( $0.125 \mu\text{m}$ ), as can be observed in Figure S9. The mCT results are coherent with this process, because, in time, more and larger pores appear in its characteristic “size window” ( $D > 2.7 \mu\text{m}$ ). Notably, in the reconstructed volumes a remarkable increase in porosity is observed. This is in striking contrast with proposed densification processes by Ostwald ripening, leading to a body of lower total porosity<sup>1</sup>. An alternative mechanism, based on crystallization and growth of K-struvite from the amorphous matrix might explain these experimental evidences.

It may be argued that a fraction of pores may initially form by air entrapment during mixing, whereas segregation of excess water into pores must be negligible for these formulations stoichiometric with respect to water. Pore size is limited by the tendency of large air bubbles to escape the sample, owing to the low viscosity of the slurry. A spherical or sub-spherical shape and a smooth surface would be expected, as confirmed by  $D_F = 2$  observed with SANS<sup>8</sup> (Figure S9). They might survive trapped into the pervasive amorphous gel-like precursor, but the amorphous-K-struvite transformation, which involves the progressive replacement of the amorphous fraction with a material of higher density,<sup>33</sup> and filling the space differently (because of its crystal habit<sup>7</sup>), favors their enlargement, together with the formation of new voids. As cement ages, their surface becomes more irregular, as testified by the increase in  $S_V$  and  $D_F$  with time. Similar behavior of  $D_F$  has been observed during crystallization of glass ceramics.<sup>34</sup> This process is compatible with the change in pore shape induced by the presence of K-struvite domains (rectangular in section) illustrated in Figure 1, and the increased complexity of the pore network evidenced by the increase in CD and in the corresponding skeleton (Figure S5). Nonetheless, as confirmed by the indexes of anisotropy, no oriented fabric develops, likely because of the nearly isotropic orientation of K-struvite in the cement volume. Considering the very small shrinkage of MPC ( $2.6\text{-}3.4 \times 10^{-5}$  after 28 days<sup>35,36</sup>), it is likely that this process entails a net increase in total porosity, including the range of sizes not accessed with mCT. The concurrent increase in mechanical performance (which is very steep in the first hours),<sup>2,3,8,14,37</sup> indicates that the contribution to the mechanical strength of the K-struvite network more

than counterbalances the negative impact of the increased porosity. The different time-evolution of mCT and SANS porosity points to a multiscale system, similarly to hydrated Portland cement<sup>38</sup> and rocks,<sup>39</sup> as has been confirmed in a recent study.<sup>3</sup>  $D_F$  depends on the scale of measurement, with  $2.1 < D_F < 2.55$  (ie rough surface) using mCT, and  $D_F = 2$  (ie smooth surface without fractal scaling) using SANS.<sup>6,8</sup>

This model of microstructural evolution agrees with a recently proposed reaction path, in which, in the early stages of the reaction, the gel-like amorphous precursor forms by aggregation of clusters,<sup>9-12</sup> marking a point of contact with the development of C-S-H gel in Portland cement. In both systems, the water in the mesopores exhibits similar dynamics.<sup>11</sup> It may be argued that numerical simulations, which allowed for a description of the correlation between structural parameters derived from image analysis and SANS, reaction mechanisms and mechanical properties in Portland cement,<sup>40,41</sup> might be also effectively applied to describe the microstructural evolution in MPCs and should be considered for further studies. Unlike C-S-H, structural information on intermediate precursor in MPC is still incomplete, but it cannot be excluded that condensation processes may be effective at a larger scale, similarly to C-S-H, where the interaction between nanoparticle building units was proved essential to confer the material its strength.<sup>42</sup> Such interaction is modulated by the mutating chemical environment, which, ultimately, drives the microstructural evolution, in a similar way as, in phosphate cements, properties and microstructural evolution depend upon the rate of change in chemical environment, as discussed in the next session.<sup>10,43</sup>

## 4.2 | Role of MgO reactivity

The amorphous-K-struvite transformation may also explain the microstructure of samples produced from MgO with different reactivity. Crystallization has been proposed to occur close to the surface of the MgO grains,<sup>13</sup> on their surface,<sup>16</sup> or also partly at random in the amorphous mass.<sup>7</sup> Recently, reaction kinetics analysis and mCT indicated that more than one process may be active during the setting reaction, with each single contribution changing in time and in function of the mix formulation.<sup>7,12,17</sup> Because MgO annealed at lower temperature possesses a higher specific surface area, a more reactive MgO should favor the development of more K-struvite nuclei, as confirmed by higher initial crystallization rates.<sup>7,12</sup> According to the mechanism of microstructural evolution described above, it may be argued that with more crystals, more pores (with  $D > 2.7 \mu\text{m}$ ) should form as it is, in fact, observed (8728, 5161 and 4734 in the VOI of the samples MPC\_1500\_15 days, MPC\_1550\_15 days and MPC\_1600\_15 days, respectively), and illustrated in Figure 2. Most of the difference is in the number of small pores (between 100 and  $200 \mu\text{m}^3$ ), which also give a higher



contribution to the  $S_V$ . From a qualitative standpoint, the fact that  $S_V$  increases more quickly with porosity in the samples MPC\_1500 with respect to the samples MPC\_1550 (see Table 1 and graphical representation in Figure S10), confirms that smaller pores are contributing to porosity in higher number in the sample MPC\_1500 (lower sintering temperature).

On one side, cements with higher porosity are obtained with more reactive MgO (lower sintering temperature), on the other, they show a lower content of K-struvite (Table 2) and are less performant.<sup>2,8,12</sup> This happens because K-struvite domains grow, on average, smaller, although higher in number. Higher reactivity of MgO has been already reported to hinder the development of a network of sufficiently large K-struvite individuals, decreasing the strength.<sup>2</sup> This process has been recently explained in terms of reaction kinetics, by considering that increasing the reactivity of MgO shifts the reaction toward kinetic control, which favors the formation of a large amount of amorphous phase/s and a fast evolution of pH.<sup>12</sup> With more water already bound in the products, crystallization of K-struvite is slowed down, and eventually frustrated, by the consequent decrease in ion mobility.

### 4.3 | Texture of MPCs

The observed alignment of [111]-MgO and [002]-K-struvite directions, although limited to a fraction of crystallites, might suggest a topotactic relationship. Thermodynamic and kinetic considerations indicated that, in MPCs, nucleation of the products may also occur at the surface of the MgO grains.<sup>12</sup> Several experimental and theoretical evidences indicated that, in a range of pH conditions (from 2 to 7), the MgO (111) faces are more represented after dissolution,<sup>44–48</sup> these are also the planes over which (0001) planes of Mg(OH)<sub>2</sub> (as first dissolution product) are known to grow, because of a topotactic relationship between the two. Notably, struvite has been documented to crystallize on the Mg(OH)<sub>2</sub> (0001) surfaces,<sup>49</sup> and the crystal morphology indicates that crystals lay with the (001) faces parallel to the Mg(OH)<sub>2</sub> (0001),<sup>50,51</sup> again suggesting some topotactic relationship. Therefore, it can be conjectured that a fraction of K-struvite might also form by consuming the Mg(OH)<sub>2</sub> intermediate, therefore, the crystals will lay with their (002) faces parallel to the (111) of MgO. To date, evidences of formation of the hydroxide at the surface of MgO during dissolution, or in the early reaction products of MPC, are conflicting<sup>7–9,11,12,14,46,47,52,53</sup>. To clarify this aspect, further investigations are needed.

A detailed analysis of the toughening mechanisms in MPC is outside the scope of this paper, but the characterization of the microstructure, its time-evolution and the sample texture, might provide some useful insights into it. The cement strength arises thanks to the interplay between several factors, such as the development of an interlocked lath-shaped microstructure, the amount of K-struvite, its

crystallographic preferred orientation, and the evolution of the pore network. The first is a well-known toughening mechanism in ceramic materials,<sup>54,55</sup> bringing advantages with respect to crack deflection and propagation<sup>56</sup>; the second may be also considered beneficial, because usually crystalline solids perform better than their amorphous counterpart.<sup>54,57</sup> Conversely, in brittle solids, pores and cracks act as stress concentrators,<sup>58</sup> with detrimental effect on performance. Using our elaboration conditions, the MPC sample exhibited a smooth texture, which may be considered positively. The same is for the negligible anisotropy shown by the pore network. Texture weakness is enough to prevent preferred crack propagation paths in the material; for example, nearly randomly oriented crystals enhance crack deflection.<sup>59</sup> On the other hand, the residual compressive stress, detected with Combined Analysis, and recognised to play a role in the strengthening of some glass-ceramics,<sup>55,60</sup> has been found rather low (<20 MPa). To date, no report gives account of the influence of the above parameters on the properties of MPCs.

## 5 | CONCLUSIONS

The new evidences about the time-evolution of microstructure in MPCs, here provided, suggest that previous predictive models of cement properties based on densification processes,<sup>1</sup> should be reconsidered. Moreover, the connection between microstructural evolution, texture, and properties corroborating theories on reaction mechanisms, is of help for a more effective design of products for applications.

The following conclusions can be drawn from the present work:

1. 3D quantitative image analysis from mCT, indicates a coarsening of the sample microstructure in time. This process was driven by the crystallization of K-struvite from the amorphous/paracrystalline precursor, and involved the progressive build-up of a network of elongated/tabular crystals with density higher than the amorphous counterpart. The development of such interlocked lath-shaped microstructure is considered the main toughening mechanism. Its contribution to the reported increase in mechanical strength with time, must thus largely overcome the negative impact of the increase in porosity.
2. The pore shape changes during the reaction becoming more irregular, whereas a more complex pore network with higher connectivity density and specific surface area, develops. This, together with the observed microstructural development, the lower porosity of samples obtained with less reactive MgO, their higher content in K-struvite, and, their already reported better performance, is in agreement with previously proposed reaction mechanisms.

3. The alignment of [111]-MgO and [002]-K-struvite directions for a fraction of crystallites, derived from texture analysis, indicated that, at least in part, the surface of MgO grains favored nucleation of K-struvite, suggesting a topotactic relationship and the presence of more than one crystallization mechanism. Overall, the texture of the sample is weak, indicating a nearly random orientation of crystallites, together with a low anisotropy of the pore network, they bring benefits with respect to crack propagation.

## ACKNOWLEDGMENTS

The authors acknowledge Ines Puente Orench for the support during the neutron experiment and the CERIC-ERIC Consortium for the access to Synchrotron experimental facility and financial support.

## ORCID

Alberto Viani  <https://orcid.org/0000-0002-6019-1094>

## REFERENCES

- Ma H, Xu B, Liu J, Pei H, Li Z. Effects of water content, magnesia-to-phosphate molar ratio and age on pore structure, strength and permeability of magnesium potassium phosphate cement paste. *Mater Des.* 2014;64:497–502.
- Li Y, Sun J, Li J, Shi T. Effects of fly ash, retarder and calcination of magnesia on properties of magnesia-phosphate cement. *Adv Cem Res.* 2015;27:373–80.
- Lee K-H, Yoon H-S, Yang K-H. Tests on magnesium potassium phosphate composite mortars with different water-to-binder ratios and molar ratios of magnesium-to-phosphate. *Constr Build Mater.* 2017;146:303–11.
- Ibrahim WA, Sibak HA, Abadir MF. Preparation and characterization of chemically bonded phosphate ceramics (CBPC) for encapsulation of harmful waste. *J Am Sci.* 2011;7:543–8.
- Walling SA, Provis JL. Magnesia-based cements: a journey of 150 years, and cements for the future? *Chem Rev.* 2016;116:4170–204.
- Viani A, Radulescu A, Pérez-Estébanez M. Characterisation and development of fine porosity in magnesium potassium phosphate ceramics. *Mater Lett.* 2015;161:628–30.
- Viani A, Pérez-Estébanez M, Pollastri S, Gualtieri AF. In situ synchrotron powder diffraction study of the setting reaction kinetics of magnesium-potassium phosphate cements. *Cem Concr Res.* 2016;79:344–52.
- Viani A, Sotiriadis K, Šašek P, Appavou M-S. Evolution of microstructure and performance in magnesium potassium phosphate ceramics: role of sintering temperature of MgO powder. *Ceram Int.* 2016;42:16310–6.
- Viani A, Mali G, Mácová P. Investigation of amorphous and crystalline phosphates in magnesium phosphate ceramics with solid-state <sup>1</sup>H and <sup>31</sup>P NMR spectroscopy. *Ceram Int.* 2017;43:6571–9.
- Mácová P, Viani A. Investigation of setting reaction in magnesium potassium phosphate ceramics with time resolved infrared spectroscopy. *Mater Lett.* 2017;205:62–6.
- Viani A, Zbiri M, Bordallo HN, Gualtieri AF, Mácová P. Investigation of the setting reaction in magnesium phosphate ceramics with quasielastic neutron scattering. *J Phys Chem C.* 2017;121:11355–67.
- Viani A, Mácová P. Polyamorphism and frustrated crystallization in the acid-base reaction of magnesium potassium phosphate cements. *Cryst Eng Comm.* 2018;20:4600–13.
- Soudée E, Péra J. Mechanism of setting reaction in magnesia-phosphate cements. *Cem Concr Res.* 2000;30:315–21.
- Viani A, Gualtieri AF. Preparation of magnesium phosphate cement by recycling the product of thermal transformation of asbestos containing wastes. *Cem Concr Res.* 2014;58:56–66.
- Taris A, Grosso M, Brundu M, Guida V, Viani A. Application of combined multivariate techniques for the description of time-resolved powder X-ray diffraction data. *J Appl Crystallogr.* 2017;50:451–61.
- Ding Z, Dong B, Xing F, Han N, Li Z. Cementing mechanism of potassium phosphate based magnesium phosphate cement. *Ceram Int.* 2012;38:6281–8.
- Viani A, Sotiriadis K, Lanzafame G, Mancini L. 3D microstructure of magnesium potassium phosphate ceramics from X-ray tomography: new insights into the reaction mechanisms. *J Mater Sci.* 2019;54:3748–60.
- Ding Z, Li Z. Effect of aggregates and water contents on the properties of magnesium phospho-silicate cement. *Cem Concr Compos.* 2005;27:11–8.
- Maire E, Withers PJ. Quantitative X-ray tomography. *Int Mater Rev.* 2014;59:1–43.
- Wilkins SW, Gureyev TE, Gao DC, Pogany A, Stevenson AW. Phase-contrast imaging using polychromatic hard X-rays. *Nature.* 1996;384:335–8.
- Brun F, Mancini L, Kasae P, Favretto S, Dreossi D, Tromba G. Pore3D: a software library for quantitative analysis of porous media. *Nucl Instr Methods Phys Res Sect A Accel Spectrometers Detect Assoc Equip.* 2010;615:326–32.
- Schindelin J, Arganda-Carreras I, Frise E, Kaynig V, Longair M, Pietzsch T, et al. Fiji: an open-source platform for biological-image analysis. *Nat Methods.* 2012;9:676–82.
- Bear J. Dynamics of fluids in porous media. *Soil Sci.* 1975;120:162–3.
- Lindquist WB, Venkatarangan A. Investigating 3D geometry of porous media from high resolution images. *Phys Chem Earth Part A Solid Earth Geod.* 1999;24:593–9.
- Brun F, Dreossi D. Efficient curve-skeleton computation for the analysis of biomedical 3d images—biomed 2010. *Biomed Sci Instrum.* 2010;46:475–80.
- Gražulis S, Chateigner D, Downs RT, Yokochi A, Quirós M, Lutterotti L, et al. Crystallography open database—an open-access collection of crystal structures. *J Appl Crystallogr.* 2009;42:726–9.
- Viani A, Gualtieri A, Puente Orench I, Zucali M. Texture analysis of magnesium potassium phosphate ceramics. Grenoble, France: Institut Laue-Langevin (ILL); 2016.
- Chateigner D. Combined analysis. Hoboken, NJ: John Wiley & Sons; 2013.
- Lutterotti L. Total pattern fitting for the combined size-strain-stress-texture determination in thin film diffraction. *Nucl Instr Methods Phys Res Sect B Beam Interact with Mater Atoms.* 2010;268:334–40.
- Matthies S, Vinel GW, Helming K. Standard distributions in texture analyses. Berlin: Akademie-Verlag; 1987.

31. Chateigner D. Reliability criteria in quantitative texture analysis with experimental and simulated orientation distributions. *J Appl Crystallogr.* 2005;38:603–11.
32. Viani A, Sotiriadis K, Kumpová I, Mancini L, Appavou M-S. Microstructural characterization of dental zinc phosphate cements using combined small angle neutron scattering and microfocus X-ray computed tomography. *Dent Mater.* 2017;33:402–17.
33. Navrotsky A. Energetic clues to pathways to biomineralization: precursors, clusters, and nanoparticles. *Proc Natl Acad Sci.* 2004;101:12096–101.
34. Butusov OB, Meshalkin VP, Orlova LA, Shchegoleva NE, Kabanov AN. Texture and fractal analysis of silica-alumina glass ceramics. *Theor Found Chem Eng.* 2016;50:188–93.
35. Li Y, Chen B. Factors that affect the properties of magnesium phosphate cement. *Constr Build Mater.* 2013;47:977–83.
36. Li J, Zhang W, Cao Y. Laboratory evaluation of magnesium phosphate cement paste and mortar for rapid repair of cement concrete pavement. *Constr Build Mater.* 2014;58:122–8.
37. Park JW, Kim KH, Ann KY. Fundamental properties of magnesium phosphate cement mortar for rapid repair of concrete. *Adv Mater Sci Eng.* 2016;2016:1–7.
38. Winslow D, Bukowski JM, Young JF. The fractal arrangement of hydrated cement paste. *Cem Concr Res.* 1995;25:147–56.
39. Anovitz LM, Cole DR. Characterization and analysis of porosity and pore structures. *Rev Mineral Geochem.* 2015;80:61–164.
40. Ioannidou K, Pellenq RJ-M, Del Gado E. Controlling local packing and growth in calcium–silicate–hydrate gels. *Soft Matter.* 2014;10:1121–33.
41. Ioannidou K, Krakowiak KJ, Bauchy M, Hoover CG, Masoero E, Yip S, et al. Mesoscale texture of cement hydrates. *Proc Natl Acad Sci.* 2016;113:2029–34.
42. Ioannidou K, Kanduč M, Li L, Frenkel D, Dobnikar J, Del Gado E. The crucial effect of early-stage gelation on the mechanical properties of cement hydrates. *Nat Commun.* 2016;7:12106.
43. Sotiriadis K, Mácová P, Mazur AS, Tolstoy PM, Viani A. A solid state NMR and in-situ infrared spectroscopy study on the setting reaction of magnesium sodium phosphate cement. *J Non Cryst Solids.* 2018;498:49–59.
44. Geysersmans P, Finocchi F, Goniakowski J, Hacquart R, Jupille J. Combination of (100), (110) and (111) facets in MgO crystals shapes from dry to wet environment. *Phys Chem Chem Phys.* 2009;11:2228.
45. Jordan G, Higgins SR, Eggleston CM. Dissolution of the periclase (001) surface; a scanning force microscope study. *Am Mineral.* 1999;84:144.
46. Berry AJ, Fraser DG, Grime GW, Craven J, Sleeman JT. The hydration and dissolution of periclase. *Mineral Mag.* 1998;62A:158–9.
47. Mejias JA, Berry AJ, Refson K, Fraser DG. The kinetics and mechanism of MgO dissolution. *Chem Phys Lett.* 1999;314:558–63.
48. Hacquart R, Jupille J. Hydrated MgO smoke crystals from cubes to octahedra. *Chem Phys Lett.* 2007;439:91–4.
49. Hövelmann J, Putnis CV. In situ nanoscale imaging of struvite formation during the dissolution of natural brucite: implications for phosphorus recovery from wastewaters. *Environ Sci Technol.* 2016;50:13032–41.
50. Abbona F, Boistelle R. Growth morphology and crystal habit of struvite crystals ( $\text{MgNH}_4\text{PO}_4 \cdot 6\text{H}_2\text{O}$ ). *J Cryst Growth.* 1979;46:339–54.
51. Abbona F, Calleri M, Ivaldi G. Synthetic struvite,  $\text{MgNH}_4\text{PO}_4 \cdot 6\text{H}_2\text{O}$ : correct polarity and surface features of some complementary forms. *Acta Crystallogr Sect B Struct Sci.* 1984;40:223–7.
52. Wogelius RA, Refson K, Fraser DG, Grime GW, Goff JP. Periclase surface hydroxylation during dissolution. *Geochim Cosmochim Acta.* 1995;59:1875–81.
53. Liu P, Kendelewicz T, Brown GE, Parks GA. Reaction of water with MgO(100) surfaces. Part I. *Surf Sci.* 1998;412–413:287–314.
54. Serbena FC, Mathias I, Foerster CE, Zanotto ED. Crystallization toughening of a model glass-ceramic. *Acta Mater.* 2015;86:216–28.
55. Apel E, Deubener J, Bernard A, Höland M, Müller R, Kappert H, et al. Phenomena and mechanisms of crack propagation in glass-ceramics. *J Mech Behav Biomed Mater.* 2008;1:313–25.
56. Mecholsky J. Toughening in glass ceramic through microstructural design. In: Bradt RC, Evans AG, Hasselman D, Lange FF, editors. *Fracture mechanics of ceramics*, vol. 6. New York, NY: Plenum Press, 1983; p. 165.
57. Bellucci D, Cannillo V, Sola A. An overview of the effects of thermal processing on bioactive glasses. *Sci Sinter.* 2010;1:307–20.
58. Rice RW. Pores as fracture origins in ceramics. *J Mater Sci.* 1984;19:895–914.
59. Hutchinson JW. Mechanisms of toughening in ceramics. In: Germain P, Piau M, Caillerie D, editors. *Theoretical and applied mechanics*. Amsterdam: Elsevier Science Publishers, 1989; p. 454.
60. Freiman SW, Hench LL. Effect of crystallization on the mechanical properties of  $\text{Li}_2\text{O-SiO}_2$  glass-ceramics. *J Am Ceram Soc.* 1972;55:86–90.

## SUPPORTING INFORMATION

Additional supporting information may be found online in the Supporting Information section at the end of the article.

**How to cite this article:** Viani A, Lanzafame G, Chateigner D, et al. Microstructural evolution and texture analysis of magnesium phosphate cement. *J Am Ceram Soc.* 2019;00:1–11. <https://doi.org/10.1111/jace.16782>